Modeling Cracks of Reinforced Concrete Slabs under Fire Conditions

Feiyu Liao[1] and Zhaohui Huang, M.ASCE[2]

Abstract: Under fire conditions, the formation of large cracks within reinforced concrete floor slabs may significantly reduce the fire resistance of buildings. At present very little research has been done for modeling integrity failure of reinforced concrete slabs in fire. In this paper a nonlinear hybrid finite-element (FE) model has been developed to predict the large cracks formed in RC floor slabs in fire. The developed model was validated using the previous tested results. The nonlinear model reported in this paper can be used for assessing the integrity failure of the floor slabs in fire. **DOI: [10.1061/(ASCE)ST.1943-541X.0001996.](#)** *This work is made available under the terms of the Creative Commons Attribution 4.0 International license, http://creativecommons.org/licenses/by/4.0/.*

Author keywords: Integrity failure; Reinforced concrete slabs in fire; Individual crack; Smeared crack; Extended finite-element method; Concrete and masonry structures.

Introduction

Concrete floor slabs play a key role for the fire resistance of composite buildings. Floor slabs not only support gravity loading, but are also important in forming membrane action within the floor slabs (Bentley et al. 1996; Huang et al. 2003; Izzuddin and Elghazouli 2004; Foster 2006; Bailey and Toh 2007). Especially at very high temperatures, the floor slab becomes the main load-bearing element, and the floor loads are carried largely because tensile membrane forces developed mainly in the reinforcing steel bars (Huang et al. 2003). However, under fire conditions, reinforced concrete slabs are subjected to large deformation. This generates large individual cracks within the floor slabs. This phenomenon was reported from some slab's fire tests (Bailey and Toh 2007). Those large individual cracks within the floor slabs will affect the fire exposure condition on the reinforcing steel bar of floor slabs, resulting in the premature failure of those reinforcing steel bars. Moreover, the integrity failure of the floor slabs results because of large individual cracks. And fire could spread from floor to floor through such large cracks. Hence, for performance-based fire safety design, it is important to predict the opening of large cracks within the floor slabs for assessing the integrity of floor slabs as well as structural stability of the whole building.

In the past, a large number of numerical studies have been carried out to predict the behaviors of concrete slabs at both ambient and high temperatures (Huang et al. 2003; Lim et al. 2004; Kodur and Bisby 2005; Zhang and Bradford 2007; Yu and Huang 2008; Shakya and Kodur 2015; Kodur and Shakya 2017). In these studies the continuum approach was adopted for the most of the numerical models, in which the cracks within the concrete slabs were assumed to smear over the whole slabs. For modeling concrete cracking, many researchers adopted the smeared crack or discrete-cracking models. However, it is obvious that the model using smeared cracking approach cannot identify individual cracks and calculate their openings within concrete floor slabs. If the discrete-cracking model is used, the cracks are assumed to form between the boundaries of meshes. This can cause mesh bias, and remesh for the analysis is needed. In order to avoid the remeshing, the extended finite-element method (XFEM) was developed (Belytschko and Black 1999), which is based on the theory of partition of unity (Melenk and Babuŝka 1996). In recent years, XFEM method has been used for many numerical procedures, such as cohesive-zone models (Wells and Sluys 2001), multiple cracks in brittle materials (Budyn et al. 2004), and intersecting cracks (Daux et al. 2000). An XFEM library was presented by Bordas et al. (2007), and a software, *PERMIX*, for multiscale modeling of cracks in material was developed by Talebi et al. (2014).

For modeling the strong discontinuity of a plate/shell element, an XFEM Mindlin-Reissner plate element was introduced by Dolbow et al. (2000). An XFEM shell formulation was employed by Areias and Belytschko (2005) to trace arbitrary crack propagations in shell structures that include both geometrical and material nonlinearities. The XFEM method for thin cracked plates with Kirchhoff-Love theory was developed by Lasry et al. (2010). Recently, Xu et al. (2013) adopted XFEM formulation for the yield line analyses of RC floor slabs. A substructured finite-element (FE) shell/extended finite-element–three-dimensional (XFE-3D) formulation was proposed by Wyart et al. (2007) for crack analysis in thin-walled structures, in which the FE-domain was discretized with shell elements whereas the XFEM-domain was modeled with 3D solid elements so that the computational cost could be reduced when compared with the complicated 3D XFEM. The authors (Liao and Huang 2015) also developed a two-dimensional (2D) XFEM model to predict large cracks in RC beams in fire.

As mentioned previously, for modeling plate/shell elements, all XFEM models were limited to assume an initial through-the-thickness crack presented within a plate (or shell). The models do not have the capability to predict the cracks' formation and propagations within RC floor slabs. Also, these models do not consider temperature's influence. At present, very few XFEM models have been developed for modeling reinforced concrete floor slabs in fires.

[1]Professor, College of Transportation and Civil Engineering, Fujian Agriculture and Forestry Univ., Fuzhou 350002, P.R. China. E-mail: liaofy@tsinghua.edu.cn

[2]Reader, Dept. of Civil and Environmental Engineering, College of Engineering, Design and Physical Science, Brunel Univ., Uxbridge, Middlesex UB8 3PH, U.K. (corresponding author). E-mail: zhaohui.huang@brunel.ac.uk

The integrity failure of floor slabs may result from large individual cracks formed within floor slabs when the slabs are deformed largely. Therefore, for structural engineers who carry out the performance-based fire safety design for reinforced concrete and composite buildings, it is highly desired to have numerical models that can be used to predict the large cracks' opening in the floor slabs. Previous research (Huang et al. 2003; Izzuddin and Elghazouli 2004; Foster 2006; Bailey and Toh 2007) indicated that the smeared crack model can predict the large deformation of floor slabs with reasonably good accuracy. However, concrete is a brittle material; some individual large cracks can be generated within the largely deformed floor slabs. The shortcoming of the smeared crack model is that the model cannot calculate the large cracks' opening in floor slabs. At present, according to the authors' knowledge, there are no available XFEM plate element models that can be used to predict the formation and propagation of individual large cracks in RC floor slabs. Also XFEM models are more computationaly demanding.

Hence, the aim of the research is developing a nonlinear finite-element model to predict the individual large cracks' opening in RC slabs at elevated temperatures. In this nonlinear procedure, a RC slab is modeled as an assembly of three different elements, which are plain concrete plate, reinforcing steel bar, and bond-link elements. In order to consider the temperature gradient along the thickness of the slab, the plate element of plain concrete was subdivided into layers. In order to predict the cracks' opening, a hybrid numerical procedure was developed. The procedure combines a smeared crack model with an XFEM model. The proposed model has the advantages of both smeared crack and XFEM models for modeling global structural behavior and localized cracking failure of the floor slabs in fire. The original contributions of this paper are:

- A hybrid finite-element procedure, combining the advantages of both smeared crack model and XFEM, was developed. For defining the shift from the smeared crack model to delayed XFEM (D-XFEM), a robust criterion is proposed. The new procedure is computationally very efficient, because only the elements accommodating the through-the-thickness cracks need to be enriched.
- The model developed in this paper takes into account the effects of temperatures induced under fire conditions. For the D-XFEM plain concrete elements, a layer procedure was adopted for representing the temperature distribution along the thickness of slabs. The model takes into account the thermal expansions of materials, the properties of the bond between the concretes and steel bars, and the material properties at elevated temperatures.

Nonlinear Numerical Procedure

Fig. 1(a) shows that a RC slab is represented as an assembly of three different elements which are plain concrete, reinforcing steel bar, and bond-link elements. For modeling plain concrete slabs, a nine-node higher-order isoparametric thick plate element is used (Huang et al. 2003). The model considers both geometric and material nonlinearities. The reinforcing steel bar is modeled using a three-node beam element. As shown in Fig. 1(b), a two-node bond-link element is used for modeling the bond characteristics between the reinforcing steel bar and concrete. One three-node steel bar element is connected to the plain concrete element using three bond-link elements. In this research, a common reference plane is defined at the midsurface of the concrete slab element. All nodes of different types of elements are located at the reference plane. Position of reference plane is assumed to be fixed during the analysis. The two connected nodes, a concrete node and a steel bar node,
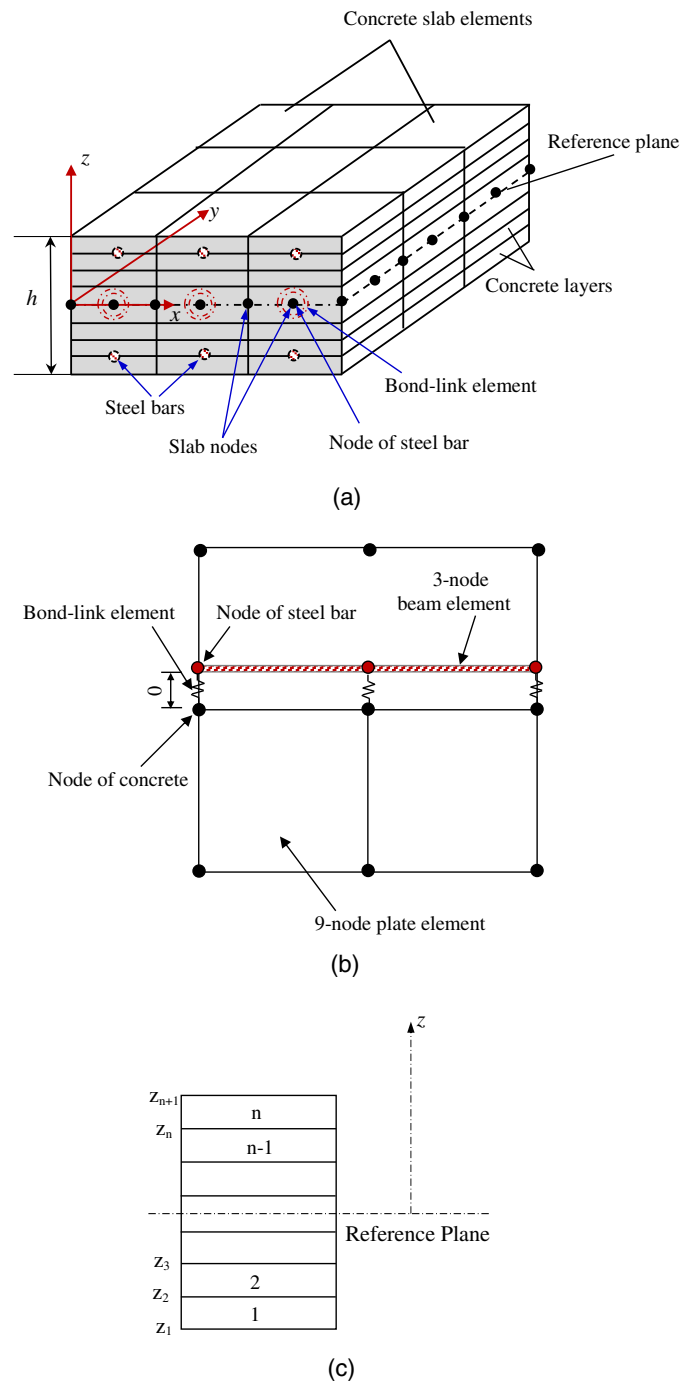

Fig. 1. Finite-element model of reinforced concrete slab: (a) layered reinforced concrete slab element; (b) concrete, steel bar, and bond-link element; (c) division of concrete slab element into layers

originally occupy the same location at the reference plane in the finite-element mesh of an undeformed structure [Fig. 1(a)].

For considering the temperature influence, the plain concrete slab elements are divided into layers along the thickness direction [Fig. 1(c)]. In this model, it is assumed that there is no slip between each layer. The stress state within each layer is plane stress. Therefore, each layer has different temperature and material properties and thermal expansions.

As mentioned before, the nonlinear procedure presented here is a hybrid FE procedure that combines the smeared crack model with XFEM. For modeling of crack evolution at the earlier stage of the
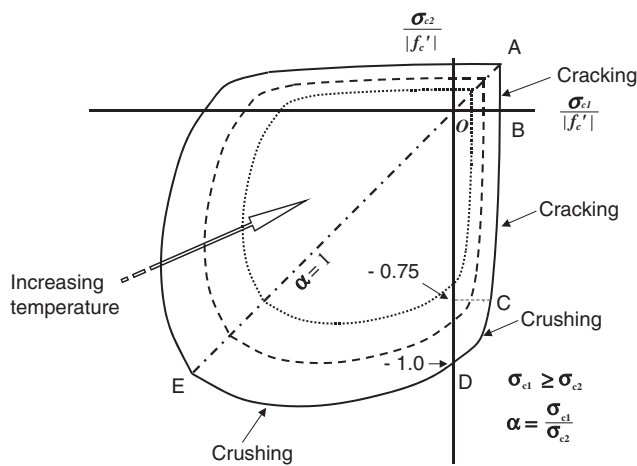
Fig. 2. Biaxial failure envelope of concrete at elevated temperatures

Fig. 3. Nine-node quadrilateral element crossed by a crack Γ_d

analysis, the smeared crack model is used in which the cracks are formed layer by layer along the thickness of the plain concrete slab elements. At the later stage of the analysis, because the slab elements are largely deformed, the delayed XFEM (D-XFEM) is used to calculate the individual through-the-thickness cracks' opening within the elements. The model cannot be used for predicting the spalling of concrete for RC slabs in fire.

For the smeared crack model, a temperature-dependent biaxial failure envelope of concrete was used (Fig. 2). The failure envelope is based on the model proposed by Kupfer and Gerstle (1973) at ambient temperature. The developed model was used to determine the failure characteristics (such as cracking or crushing of concrete) at each integration point. In this concrete failure envelope, the area enclosed by the failure envelope decreased with increasing temperatures. As shown in Fig. 2, the failure surfaces of the biaxial strength envelope were divided into four regions, which depended on the stress state as represented by the principal stress ratio $\alpha = \sigma_{c1}/\sigma_{c2}$. Compressive stresses were assumed to be negative and tensile stresses positive, and the principal directions were chosen so that $\sigma_{c1} \geq \sigma_{c2}$ algebraically. Within this model the initiation of cracking or crushing at any location occurred when the concrete principal stresses reached one of the failure surfaces.

Before cracking or crushing occurs, the integral concrete was assumed to be isotropic, homogeneous, and linearly elastic. A smeared crack model was adopted in which a cracking at any Gauss point was identified when the concrete principal stress reached one of the failure surfaces, either in the biaxial tension region (Segment AB) or in the combined tension-compression region (Segment BC) shown in Fig. 2.

After the initiation of cracking in a single direction, the concrete was treated as an orthotropic material with principal axes normal and parallel to the crack direction. The concrete parallel to the crack was capable of resisting both tensile and compressive stresses. When it was subjected to tension, linear elastic behavior was assumed, and when the concrete parallel to the crack was subjected to compression, the uniaxial stress-strain relationship was applied. Upon further loading of singly cracked concrete, a second set of cracks could be formed in the direction normal to the first set of smeared cracks. Therefore, if the stress in that direction was less than concrete tensile strength f_t', then concrete remained singly cracked. If it was greater than f_t', then the second set of cracks was formed. After crushing, concrete was assumed to lose all stiffness. Because the elements were subdivided into different layers over the thickness, the layer-by-layer failure based on stress levels
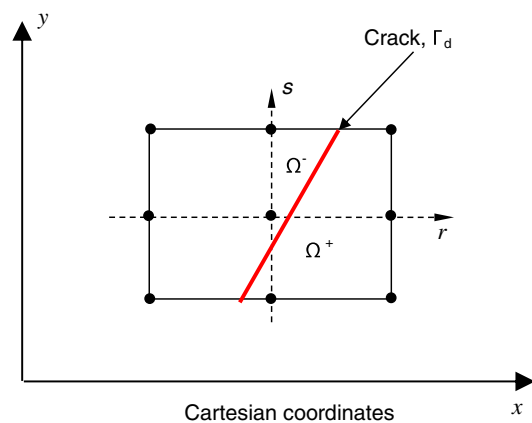
at Gauss points could be simulated in the smeared crack model. The details of the smeared crack model used in this study can be found in Huang et al. (2003).

Layered Concrete Elements with D-XFEM Model

As previously mentioned, the D-XFEM model was introduced into the plain concrete slab element for predicting the opening of large cracks within the largely deformed RC floor slabs under fire conditions.

Crack Model with D-XFEM

Stiffness Matrix of an Element, K. The development of an element stiffness matrix **K** for the concrete slab element with D-XFEM is presented in this section. For modeling the individual large cracks within the plain concrete element, the partition of unity was used. The field of displacement is represented as the sum of the fields of regular displacement and enrichment displacement (Moës et al. 1999). As shown in Fig. 3, a nine-node quadrilateral element crossed by a crack (Γ_d) can be divided into two parts, which are described as Ω^+ and Ω^- on the different sides of the crack. The displacement field **u** has a continuous regular displacement field $\mathbf{u}_{cont}$ and a discontinuous displacement field $\mathbf{u}_{dis}$:

$$\mathbf{u} = \mathbf{u}_{cont} + \mathbf{u}_{dis} = \sum_1^9 N_i \mathbf{u}_i + \sum_1^9 N_i \Psi_i(\mathbf{x}) \mathbf{a}_i \quad (1)$$

where N_i = shape function; $\mathbf{u}_i$ = regular node displacement; $\mathbf{a}_i$ = additional node displacement to represent the discontinuity; and $\Psi_i(\mathbf{x})$ = enrichment function

$$\Psi_i(\mathbf{x}) = sign(x) - sign(x_i) \quad (i = 1 \sim 9) \quad (2)$$

where $sign$ is the sign function, defined as

$$sign(x) = \begin{cases} +1 & \text{if } x \in \Omega^+ \\ -1 & \text{if } x \in \Omega^- \end{cases} \quad (3)$$

The $sign$ function given in Eq. (3) is shifted by $sign(x_i)$. According to Zi and Belytschko (2003), using the shifted $sign$ function can result in the vanishing of the enrichment displacement field outside the enhanced element. In addition, the shifted enhancement function also allows the total nodal displacement to be obtained explicitly in the model, rather than only the regular part of XFEM displacement. This makes the compatibility of total nodal displacements of plain concrete element and steel bar element feasible.
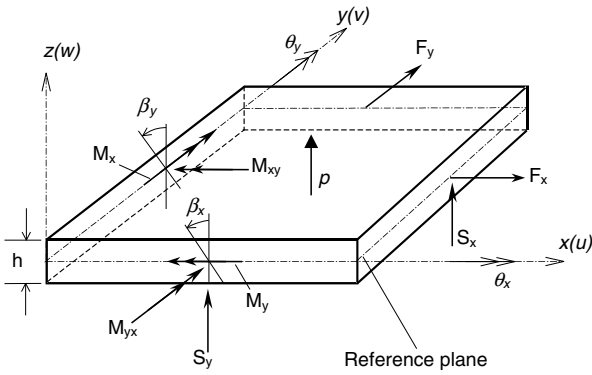
Fig. 4. Notation used for plate element

$$\mathbf{u}_i = \hat{\mathbf{u}}_m + \hat{\mathbf{u}}_p = [\hat{\mathbf{u}}_m^T \ \hat{\mathbf{u}}_p^T]^T$$
$$= [u_1^u v_1^u u_2^u v_2^u \dots u_9^u v_9^u w_1^u \theta_{x1}^u \theta_{y1}^u w_2^u \theta_{x2}^u \theta_{y2}^u \dots w_9^u \theta_{x9}^u \theta_{y9}^u]^T \quad (4)$$

$$\mathbf{a}_i = \hat{\mathbf{a}}_m + \hat{\mathbf{a}}_p = [\hat{\mathbf{a}}_m^T \ 0]^T$$
$$= [u_1^a v_1^a u_2^a v_2^a \dots u_9^a v_9^a 000000 \dots 000]^T \quad (5)$$

where u_i^u and v_i^u = regular in-plane nodal displacements; w_i^u = regular out-plane nodal displacements; θ_{xi}^u and θ_{yi}^u = regular nodal rotations; and u_i^a and v_i^a = enriched in-plane nodal displacements, respectively.

When a crack forms in a plate slab element, the plate displacements (Fig. 4) can be calculated using Eq. (6) based on Mindlin-Reissner assumptions:

$$u = -\beta_x z + (u_0^u + u_0^a)$$
$$v = -\beta_y z + (v_0^u + v_0^a)$$
$$w = w_0 \quad (6)$$

where u_0^u and v_0^u = regular in-plane displacements; u_0^a, v_0^a = enriched in-plane displacements, respectively; β_x and β_y = regular rotations with respect to y and x axes, respectively; and w_0 = regular out-of-plane displacement along the z coordinate (Fig. 4).

If the Von Karman assumptions are introduced and the large deformation is considered, the strain of a plate element with enriched in-plane displacements can be expressed as

Hence, the bond-link element can be used to link the plain concrete element and steel bar element in a conventional way.

As shown in Fig. 4, there are five degrees of freedom (DOFs) for each node of the slab element: related to the local coordinates x, y, z, the translational degrees of freedom are u, v, w, and rotational degrees of freedom are θ_x, θ_y. Because the current model mainly intends to predict the in-plane opening of individual cracks and ignore the strong discontinuity in rotations, only two membrane translational DOFs (u, v) were enriched and all other DOFs (w, θ_x, θ_y) were assumed as regular. Hence, only two additional DOFs (u_i^a, v_i^a) per node were added to the nodal displacement vector. The following equations give node displacements $\mathbf{u}_i$ and $\mathbf{a}_i$ as:

$$\varepsilon = \left\{ \begin{array}{c} -z\dfrac{\partial \beta_x}{\partial x} + \dfrac{\partial u_0^u}{\partial x} \\[2mm] -z\dfrac{\partial \beta_y}{\partial y} + \dfrac{\partial v_0^u}{\partial y} \\[2mm] -z\left(\dfrac{\partial \beta_x}{\partial y} + \dfrac{\partial \beta_y}{\partial x}\right) + \left(\dfrac{\partial u_0^u}{\partial y} + \dfrac{\partial v_0^u}{\partial x}\right) \\[2mm] -\beta_x + \dfrac{\partial w_0}{\partial x} \\[2mm] -\beta_y + \dfrac{\partial w_0}{\partial y} \end{array} \right\} + \left\{ \begin{array}{c} \dfrac{1}{2}\left(\dfrac{\partial w_0}{\partial x}\right)^2 \\[2mm] \dfrac{1}{2}\left(\dfrac{\partial w_0}{\partial y}\right)^2 \\[2mm] \dfrac{\partial w_0}{\partial x}\dfrac{\partial w_0}{\partial y} \\[2mm] 0 \\[2mm] 0 \end{array} \right\} + \left\{ \begin{array}{c} \dfrac{\partial u_0^a}{\partial x} \\[2mm] \dfrac{\partial v_0^a}{\partial y} \\[2mm] \dfrac{\partial u_0^a}{\partial y} + \dfrac{\partial v_0^a}{\partial x} \\[2mm] 0 \\[2mm] 0 \end{array} \right\} = (\varepsilon_0^u + \varepsilon_L^u) + \varepsilon^a \quad (7)$$

where ε_0^u and ε_L^u = continuous strain related to small deformation and large deformation respectively; and ε^a = discontinuous strain. Because only two membrane additional DOFs (u_i^a, v_i^a) are available, ε^a only has three items related to enriched in-plane displacements (u_0^a, v_0^a), as shown in Eq. (7). The strain rate can be represented as

$$d\boldsymbol{\varepsilon} = \mathbf{B}^u d\mathbf{u}_i + \mathbf{B}^a d\mathbf{a}_i \quad (8)$$

in which $\mathbf{B}^u$ and $\mathbf{B}^a$ = transformation matrixes of the regular and enriched strain-displacement, respectively. The details for calculating $\mathbf{B}^u$ can be found in Huang et al. (2003). The enriched strain-displacement transformation matrix ($\mathbf{B}^a$) having plane membrane item only can be written as

$$\mathbf{B}^a = \begin{bmatrix} \mathbf{B}_m^a & 0 \\ \mathbf{0} & 0 \end{bmatrix} \quad (9)$$

in which $\mathbf{B}_m^a$ = enriched strain-displacement transformation matrix related to plane membrane as

$$\mathbf{B}_m^a = \Psi_i(\mathbf{x})\mathbf{LN} = \mathbf{L}\begin{bmatrix} \Psi_1(x)N_1 & 0 & \Psi_2(x)N_2 & 0 & \dots & \dots & \Psi_9(x)N_9 & 0 \\ 0 & \Psi_1(x)N_1 & 0 & \Psi_2(x)N_2 & \dots & \dots & & \Psi_9(x)N_9 \end{bmatrix} \quad (10)$$

where the matrix $\mathbf{L}$ contains differential operators; $\Psi_i(\mathbf{x})$ = enrichment function; and N_i = shape function.

Considering the thermal expansion, the total strain (ε) is the sum of both thermal and stress-related strains. As a result, the components of the Piola-Kirchhoff stress vector can be calculated as

$$\boldsymbol{\sigma} = \left\{ \begin{array}{c} \sigma_x \\ \sigma_y \\ \tau_{xy} \\ \tau_{xz} \\ \tau_{yz} \end{array} \right\} = \mathbf{D}(\boldsymbol{\varepsilon} - \boldsymbol{\varepsilon}_T) = \mathbf{D}(\mathbf{B}^u\mathbf{u}_i + \mathbf{B}^a\mathbf{a}_i - \boldsymbol{\varepsilon}_T) \quad (11)$$

where $\mathbf{D}$ = constitutive matrix of concrete. For the enriched element, three different constitutive matrixes ($\mathbf{C}^{ela}$, $\mathbf{C}_0$ and $\mathbf{C}^s$) were used to form element stiffness matrix. The expressions of $\mathbf{C}^{ela}$, $\mathbf{C}_0$, and $\mathbf{C}^s$ are written as follows:

$$\mathbf{C}^{ela} = \frac{1}{1 - \nu^2} \begin{bmatrix} E_{ct} & \nu E_{ct} & 0 \\ \nu E_{ct} & E_{ct} & 0 \\ 0 & 0 & 0.5(1-\nu)E_{ct} \end{bmatrix} \quad (12)$$

$$\mathbf{C}^0 = \begin{bmatrix} 0 & 0 & 0 \\ 0 & 0 & 0 \\ 0 & 0 & \mu G_c \end{bmatrix} \quad (13)$$

$$\mathbf{C}^s = \begin{bmatrix} \dfrac{0.5E_{ct}}{(1+\nu)} & 0 \\ 0 & \dfrac{0.5E_{ct}}{(1+\nu)} \end{bmatrix} \quad (14)$$

where E_{ct}, G_c and ν = Young's modulus, shear modulus, and Poisson's ratio of concrete, respectively; and μ = shear retention factor, with $0 < \beta \leq 1.0$.

For the enriched element, only two membrane translational DOFs (u, v) were enriched and all other DOFs (w, θ_x, θ_y) remained as regular. Hence, the element stiffness corresponding to two plane membrane DOFs (u, v), which were enriched, the elastic constitutive matrix ($\mathbf{C}^{ela}$) was adopted because the XFEM formulations introduced can automatically realize the loss of element stiffness due to cracking. In such a way the compressive material nonlinearity was ignored in the enriched element, which is justifiable after a significant crack occurring. However, the enriched elements in the current model could not deal with crack closure, which may arise when the slab is under fire conditions. Because the enriched elements were used for those elements with extensive cracking and under large deformation, the chance of large individual cracks to be closed in the later stage of a fire was relatively remote. This viewpoint is supported from previous experimental evidence (Bentley et al. 1996; Bailey and Toh 2007). Hence, for simplicity, in the current model the crack closure was ignored for the enriched elements. For the element stiffness related to nonenriched DOFs (w, θ_x, θ_y) the cracked constitutive matrix ($\mathbf{C}_0$) was employed to account for the decrease of structural stiffness and tensile stress after cracking happened. And, $\mathbf{C}^s$ was the constitutive matrix related to transverse shear.

Based on the principle of virtual work, the stiffness matrix and internal force vector of an element can be represented as

$$\boldsymbol{\psi}(\mathbf{u}) = \int_V \bar{\mathbf{B}}^T \boldsymbol{\sigma} dV - \mathbf{f}^{\text{ext}} = \mathbf{0} \quad (15)$$

where $\boldsymbol{\psi}$ = sum of external and internal generalized forces; and $\bar{\mathbf{B}}$ = strain-displacement transformation matrix.

In this study, the concrete cracking at an early stage was represented using the smeared crack model. When the slab elements were largely deformed, the XFEM formulations were adopted to predict the opening of through-the-thickness cracks within the element. At this stage, the concrete cracking within the element was relatively significant. Therefore, for the element with extended discontinuity (D-XFEM), it was reasonable to ignore the traction force between two crack faces. Hence, in Eq. (15), the regular internal force ($\mathbf{Q}^u$) is balanced by the external force ($\mathbf{f}^{\text{ext}}$), and the enriched internal force ($\mathbf{Q}^a$) must be zero, that is

$$\mathbf{Q}^u = \int_\Omega \mathbf{B}^{uT}\boldsymbol{\sigma} d\Omega = \mathbf{f}^{\text{ext}} \quad (16)$$

$$\mathbf{Q}^a = \int_{\Omega^+,\Omega^-} \mathbf{B}^{aT}\boldsymbol{\sigma} d\Omega = \mathbf{0} \quad (17)$$

Based on the principle of virtual work, the stiffness matrix of an element can be represented as

$$\mathbf{K}d\hat{\mathbf{u}} = \begin{bmatrix} \mathbf{K}^{uu} & \mathbf{K}^{ua} \\ \mathbf{K}^{au} & \mathbf{K}^{aa} \end{bmatrix} \left\{ \begin{array}{c} \mathbf{du}_i \\ \mathbf{da}_i \end{array} \right\} = \left\{ \begin{array}{c} \mathbf{f}^{\text{ext}} \\ 0 \end{array} \right\} - \left\{ \begin{array}{c} \mathbf{Q}^u \\ \mathbf{Q}^a \end{array} \right\} \quad (18)$$

where $\mathbf{K}^{uu}$ = stiffness matrix of an element that is related to regular DOFs; $\mathbf{K}^{aa}$ = stiffness matrix of an element that is related to enriched DOFs; and $\mathbf{K}^{ua} = (\mathbf{K}^{au})^T$ is related to both.

The standard element stiffness $\mathbf{K}^{uu}$ only related to regular DOFs is composed of $\mathbf{K}^{uu}_m$, $\mathbf{K}^{uu}_p$, $\mathbf{K}^{uu}_{mb}$, and $\mathbf{K}^{uu}_{mb}$ as (Huang et al. 2003)

$$\mathbf{K}^{uu} = \begin{bmatrix} \mathbf{K}^{uu}_m & \mathbf{K}^{uu}_{mb} \\ \mathbf{K}^{uu}_{bm} & \mathbf{K}^{uu}_p \end{bmatrix} \quad (19)$$

where $\mathbf{K}^{uu}_m$ = stiffness matrix related to plane membrane stress; $\mathbf{K}^{uu}_p$ = stiffness matrix related to bending and shear stresses; $\mathbf{K}^{uu}_{mb}$ and $\mathbf{K}^{uu}_{mb}$ = stiffness matrixes related to both plane membrane and bending stresses.

As mentioned above, three constitutive matrixes $\mathbf{C}^{ela}$, $\mathbf{C}_0$, and $\mathbf{C}^s$ were used to deal with enriched plane membrane DOFs, nonenriched DOFs, and transverse shear, respectively. Based on this principle, the following rules were implemented in building element stiffness matrixes: $\mathbf{C}^{ela}$ was used for calculating element stiffness matrixes that had plane membrane strain-displacement transformation matrix ($\mathbf{B}^u_m$, $\mathbf{B}^a_m$) or the nonlinear one $\mathbf{B}^u_L$; $\mathbf{C}_0$ was used for calculating element stiffness matrixes that had bending strain-displacement transformation matrix $\mathbf{B}^u_b$ only; and $\mathbf{C}^s$ was used for calculating element stiffness matrixes that had shear strain-displacement transformation matrix $\mathbf{B}^u_s$ only. By such way, $\mathbf{K}^{uu}_m$, $\mathbf{K}^{uu}_{mb}$, $\mathbf{K}^{uu}_{mb}$, and $\mathbf{K}^{uu}_p$ can be formed as follows:

$$\mathbf{K}^{uu}_m = \int_\Omega \mathbf{B}^{u\,T}_m \mathbf{C}^{ela} \mathbf{B}^u_m d\Omega = \iint_A \mathbf{B}^{u\,T}_m \left(\int \mathbf{C}^{ela} dz \right) \mathbf{B}^u_m dxdy \quad (20)$$

$$\begin{aligned} \mathbf{K}^{uu}_{mb} &= \int_\Omega \mathbf{B}^{u\,T}_m z\mathbf{C}^{ela}\mathbf{B}^u_b d\Omega + \int_\Omega \mathbf{B}^{u\,T}_m \mathbf{C}^{ela}\mathbf{B}^u_L d\Omega \\ &= \iint_A \mathbf{B}^{u\,T}_m \left(\int z\mathbf{C}^{ela} dz \right) \mathbf{B}^u_b dxdy \\ &\quad + \iint_A \mathbf{B}^{u\,T}_m \left(\int \mathbf{C}^{ela} dz \right) \mathbf{B}^u_L dxdy \end{aligned} \quad (21)$$

$$\mathbf{K}_{bm}^{uu} = \int_{\Omega} \mathbf{B}_b^{u\,T} z \mathbf{C}^{ela} \mathbf{B}_m^u d\Omega + \int_{\Omega} \mathbf{B}_L^{u\,T} \mathbf{C}^{ela} \mathbf{B}_m^u d\Omega$$

$$= \iint_A \mathbf{B}_b^{u\,T} \left(\int z\mathbf{C}^{ela} dz \right) \mathbf{B}_m^u dx dy$$

$$+ \iint_A \mathbf{B}_L^{u\,T} \left(\int \mathbf{C}^{ela} dz \right) \mathbf{B}_m^u dx dy \qquad (22)$$

$$\mathbf{K}_P^{uu} = \int_{\Omega} \mathbf{B}_b^{u\,T} z^2 \mathbf{C}^0 \mathbf{B}_b^u d\Omega + \int_{\Omega} \mathbf{B}_s^{u\,T} k\mathbf{C}^s \mathbf{B}_s^u d\Omega + \int_{\Omega} \mathbf{B}_b^{u\,T} z\mathbf{C}^{ela} \mathbf{B}_L^u d\Omega$$

$$+ \int_{\Omega} \mathbf{B}_L^{u\,T} \mathbf{C}^{ela} \mathbf{B}_L^u d\Omega + \int_{\Omega} \mathbf{B}_L^{u\,T} z\mathbf{C}^{ela} \mathbf{B}_b^u d\Omega + \int_V \hat{\mathbf{G}}^T \hat{\sigma} \hat{\mathbf{G}} dV$$

$$= \iint_A \mathbf{B}_b^{u\,T} \left(\int z^2 \mathbf{C}^0 dz \right) \mathbf{B}_b^u dx dy$$

$$+ \iint_A \mathbf{B}_s^{u\,T} \left(\int k\mathbf{C}^s dz \right) \mathbf{B}_s^u dx dy$$

$$+ \iint_A \mathbf{B}_b^{u\,T} \left(\int z\mathbf{C}^{ela} dz \right) \mathbf{B}_L^u dx dy$$

$$+ \iint_A \mathbf{B}_L^{u\,T} \left(\int \mathbf{C}^{ela} dz \right) \mathbf{B}_L^u dx dy$$

$$+ \iint_A \mathbf{B}_L^{u\,T} \left(\int z\mathbf{C}^{ela} dz \right) \mathbf{B}_b^u dx dy$$

$$+ \iint_A \hat{\mathbf{G}}^T \left(\int \hat{\sigma} dz \right) \hat{\mathbf{G}} dx dy \qquad (23)$$

In Eq. (23), $\hat{\sigma}$ is calculated as

$$\hat{\boldsymbol{\sigma}} = \begin{bmatrix} \sigma_x & \tau_{xy} \\ \tau_{xy} & \sigma_y \end{bmatrix} \qquad (24)$$

and $\hat{\mathbf{G}}$ is a matrix defined purely in terms of the coordinates as

$$\hat{\mathbf{G}} = \begin{bmatrix} \dfrac{\partial}{\partial x} & 0 & 0 \\ \dfrac{\partial}{\partial y} & 0 & 0 \end{bmatrix} \qquad (25)$$

In Eq. (18), $\mathbf{K}^{ua}$ and $\mathbf{K}^{au}$ are the stiffness matrixes related to both enriched DOFs and regular DOFs, and $\mathbf{K}^{ua}$ is involved additional nodal displacements that only have two enriched plane membrane items (u_i^a, v_i^a). Therefore, only $\mathbf{K}_m^{ua}$ and $\mathbf{K}_{bm}^{ua}$ corresponding to u_i^a, v_i^a were available, and other items in the matrix like $\mathbf{K}_{mb}^{ua}$ and $\mathbf{K}_P^{ua}$ corresponding to w^a, θ_x^a, θ_y^a should be zero, that is

$$\mathbf{K}^{ua} = \begin{bmatrix} \mathbf{K}_m^{ua} & 0 \\ \mathbf{K}_{bm}^{ua} & 0 \end{bmatrix} \qquad (26)$$

where

$$\mathbf{K}_m^{ua} = \int_{\Omega^+,\Omega^-} \mathbf{B}_m^{u\,T} \mathbf{C}^{ela} \mathbf{B}_m^a d\Omega = \iint_{A^+,A^-} \mathbf{B}_m^{u\,T} \left(\int \mathbf{C}^{ela} dz \right) \mathbf{B}_m^a dx dy \qquad (27)$$

$$\mathbf{K}_{bm}^{ua} = \int_{\Omega^+,\Omega^-} \mathbf{B}_b^{u\,T} z\mathbf{C}^{ela} \mathbf{B}_m^a d\Omega + \int_{\Omega^+,\Omega^-} \mathbf{B}_L^{u\,T} \mathbf{C}^{ela} \mathbf{B}_m^a d\Omega$$

$$= \iint_{A^+,A^-} \mathbf{B}_b^{u\,T} \left(\int z\mathbf{C}^{ela} dz \right) \mathbf{B}_m^a dx dy$$

$$+ \iint_{A^+,A^-} \mathbf{B}_L^{u\,T} \left(\int \mathbf{C}^{ela} dz \right) \mathbf{B}_m^a dx dy \qquad (28)$$

In Eq. (26), the column of zeroes will multiply three zeroes additional DOFs [$\hat{\mathbf{a}}_p = [w^a\ \theta_x^a\ \theta_y^a] = [0\,0\,0]$, see Eq. (5)].

As shown in Eq. (18), $\mathbf{K}^{au}$ will multiply $\mathbf{du}_i$ to obtain enriched internal force $\mathbf{Q}^a$, which only has items related to membrane stresses. Therefore, only $\mathbf{K}_m^{au}$ and $\mathbf{K}_{mb}^{au}$ are available and other items like $\mathbf{K}_{bm}^{au}$ and $\mathbf{K}_p^{au}$ should be zero, that is

$$\mathbf{K}^{au} = \begin{bmatrix} \mathbf{K}_m^{au} & \mathbf{K}_{mb}^{au} \\ 0 & 0 \end{bmatrix} \qquad (29)$$

in which

$$\mathbf{K}_m^{au} = \int_{\Omega^+,\Omega^-} \mathbf{B}_m^{a\,T} \mathbf{C}^{ela} \mathbf{B}_m^u d\Omega$$

$$= \iint_{A^+,A^-} \mathbf{B}_m^{a\,T} \left(\int \mathbf{C}^{ela} dz \right) \mathbf{B}_m^u dx dy \qquad (30)$$

$$\mathbf{K}_{mb}^{au} = \int_{\Omega^+,\Omega^-} \mathbf{B}_m^{a\,T} z\mathbf{C}^{ela} \mathbf{B}_b^u d\Omega + \int_{\Omega^+,\Omega^-} \mathbf{B}_m^{a\,T} \mathbf{C}^{ela} \mathbf{B}_L^u d\Omega$$

$$= \iint_{A^+,A^-} \mathbf{B}_m^{a\,T} \left(\int z\mathbf{C}^{ela} dz \right) \mathbf{B}_b^u dx dy$$

$$+ \iint_{A^+,A^-} \mathbf{B}_m^{a\,T} \left(\int \mathbf{C}^{ela} dz \right) \mathbf{B}_L^u dx dy \qquad (31)$$

$\mathbf{K}^{aa}$ = stiffness matrix related to enriched DOFs. Because only membrane DOFs were enriched

$$\mathbf{K}^{aa} = \begin{bmatrix} \mathbf{K}_m^{aa} & 0 \\ 0 & 0 \end{bmatrix} \qquad (32)$$

in which

$$\mathbf{K}_m^{aa} = \int_{\Omega^+,\Omega^-} \mathbf{B}_m^{a\,T} \mathbf{C}^{ela} \mathbf{B}_m^a d\Omega$$

$$= \iint_{A^+,A^-} \mathbf{B}_m^{a\,T} \left(\int \mathbf{C}^{ela} dz \right) \mathbf{B}_m^a dx dy \qquad (33)$$

Because the effects of elevated temperatures were included in the model, all material stiffness matrixes are temperature-dependent. As mentioned previously, in a layered slab element the temperature and material property of each layer were different, but within a layer they were constant for each temperature step. Therefore, the inner integrations $\int z^2 \mathbf{C}^0 dz$, $\int z\mathbf{C}^0 dz$, $\int z\mathbf{C}^{ela} dz$, $\int \mathbf{C}^{ela} dz$, and $\int k\mathbf{C}^s dz$ in Eqs. (20)–(33) could be carried out separately and replaced by summation over the layers along the z-axis as

$$\int z^2 \mathbf{C}^0 dz = \sum_{l=1}^n \frac{1}{3}(z_{l+1}^3 - z_l^3)\mathbf{C}_l^0 \qquad (34)$$

$$\int z\mathbf{C}^0 dz = \sum_{l=1}^n \frac{1}{2}(z_{l+1}^2 - z_l^2)\mathbf{C}_l^0 \qquad (35)$$

$$\int z\mathbf{C}^{ela} dz = \sum_{l=1}^n \frac{1}{2}(z_{l+1}^2 - z_l^2)\mathbf{C}_l^{ela} \qquad (36)$$

$$\int \mathbf{C}^{ela} dz = \sum_{l=1}^n (z_{l+1} - z_l)\mathbf{C}_l^{ela} \qquad (37)$$

$$\int k\mathbf{C}^s dz = \sum_{l=1}^n k(z_{l+1} - z_l)\mathbf{C}_l^s \qquad (38)$$

where z_l = distance from reference plane to the lth layer; $\mathbf{C}_l^{ela}$ = material stiffness matrix relating to plane stress for the lth layer;

© ASCE

04018030-6

J. Struct. Eng.

$\mathbf{C}_l^0$ = material stiffness matrix relating to bending for lth layer; $\mathbf{C}_l^s$ = material stiffness matrix relating to shearing for the lth layer; n = total number of element layers; and $k = 5/6$, a factor to take into account the influence of the nonuniform shear stress along the thickness of slabs.

Internal Force Vector of an Element, Q^e. The internal force vectors can be written as

$$\mathbf{Q}_e = \left\{ \begin{array}{c} \mathbf{Q}^u \\ \mathbf{Q}^a \end{array} \right\} \tag{39}$$

where $\mathbf{Q}^u$ and $\mathbf{Q}^a$ = regular and enriched internal force, respectively

$$\mathbf{Q}^u = \int_\Omega \mathbf{B}^{uT} \sigma d\Omega = \int_\Omega (\mathbf{B}_0^u + \mathbf{B}_L^u)^T \boldsymbol{\sigma} d\Omega = \left\{ \begin{array}{c} \mathbf{Q}_m^u \\ \mathbf{Q}_p^u \end{array} \right\} + \left\{ \begin{array}{c} 0 \\ \mathbf{Q}_L^u \end{array} \right\} \tag{40}$$

where $\mathbf{Q}_m^u$ = regular internal force related to membrane stresses; $\mathbf{Q}_p^u$ = regular internal force related to bending and shear stresses; and $\mathbf{Q}_L^u$ = regular internal force related to large deformation. Because only two membrane additional DOFs (u_i^a, v_i^a) were enriched, the enriched internal force $\mathbf{Q}^a$ only had the item $\mathbf{Q}_m^a$ related to membrane stresses and other enriched internal force vectors corresponding to DOFs (w^a, θ_x^a, θ_y^a) should have been zero. That is

$$\mathbf{Q}^a = \int_{\Omega^+, \Omega^-} \mathbf{B}^{aT} \boldsymbol{\sigma} d\Omega = \left\{ \begin{array}{c} \mathbf{Q}_m^a \\ 0 \end{array} \right\} \tag{41}$$

Let $\boldsymbol{\sigma}^p = \{\sigma_z, \sigma_x, \tau_{zx}\}^T$ and $\boldsymbol{\tau} = \{\tau_{zy}, \tau_{xy}\}^T$, so $\boldsymbol{\sigma} = \{\boldsymbol{\sigma}^p, \boldsymbol{\tau}\}^T$. Then we have

$$\mathbf{Q}_m^u = \int_\Omega \mathbf{B}_m^{uT} \boldsymbol{\sigma}^p d\Omega = \iint_A \mathbf{B}_m^{uT} \left(\int \boldsymbol{\sigma}^p dz \right) dx dy \tag{42}$$

$$\mathbf{Q}_p^u = \int_\Omega \mathbf{B}_b^{uT} z \boldsymbol{\sigma}^p d\Omega + \int_\Omega \mathbf{B}_s^{uT} \boldsymbol{\tau} d\Omega$$
$$= \iint_A \mathbf{B}_b^{uT} \left(\int z \boldsymbol{\sigma}^p dz \right) dx dy + \iint_A \mathbf{B}_s^{uT} \left(\int k \boldsymbol{\tau} dz \right) dx dy \tag{43}$$

$$\mathbf{Q}_L^u = \int_\Omega \mathbf{B}_L^{uT} \boldsymbol{\sigma}^p d\Omega = \iint_A \mathbf{B}_L^{uT} \left(\int \boldsymbol{\sigma}^p dz \right) dx dy \tag{44}$$

$$\mathbf{Q}_m^a = \int_{\Omega^+, \Omega^-} \mathbf{B}_m^{aT} \boldsymbol{\sigma}^p dV = \iint_{A^+, A^-} \mathbf{B}_m^{aT} \left(\int \boldsymbol{\sigma}^p dz \right) dx dy \tag{45}$$

where $\int \boldsymbol{\sigma}^p dz$, $\int z \boldsymbol{\sigma}^p dz$, and $\int k \boldsymbol{\tau} dz$ in Eqs. (42)–(45) can be expressed by summation over the layers and replaced as

$$\int \boldsymbol{\sigma}^p dz = \sum_{l=1}^n (z_{l+1} - z_l) \boldsymbol{\sigma}_l^p \tag{46}$$

$$\int z \boldsymbol{\sigma}^p dz = \sum_{l=1}^n \frac{1}{2} (z_{l+1}^2 - z_l^2) \boldsymbol{\sigma}_l^p \tag{47}$$

$$\int k \boldsymbol{\tau} dz = \sum_{l=1}^n k(z_{l+1} - z_l) \boldsymbol{\tau}_l \tag{48}$$
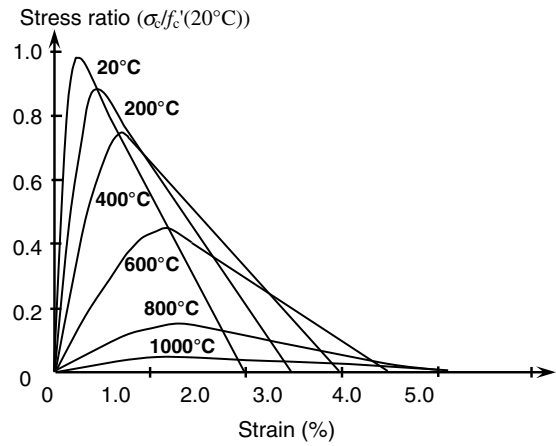

Fig. 5. Uniaxial concrete compressive stress-strain relationships at high temperature

where σ_l^p = stress vector related to plane stress in the lth layer; τ_l = stress vector relating to shearing in the lth layer; and n = total number of layers.

Constitutive Modeling of Concrete at Elevated Temperatures

In the nonlinear procedure previously described, the compressive strength of concrete is reduced at elevated temperatures. Fig. 5 shows the models proposed in EN1992-1-2 (Commission of the European Communities 2004) to calculate the uniaxial compressive strength of concrete subjected to high temperature. Also a model specified in EN1992-1-2 (Commission of the European Communities 2004) was adopted for calculating concrete thermal expansion. It was assumed that there was no thermal shear strain for concrete in the state of plane stresses. The shrinkage and creep of concrete was not considered in the model. The uniaxial tensile and compressive strengths were assumed to be related by $f_t' = 0.3321\sqrt{f_c'}$ MPa (Huang et al. 2003).

Concrete exhibits a linear elastic behavior up to its ultimate tensile capacity. Beyond this the tensile stress decreases gradually with increasing tensile strain, rather than dropping to zero abruptly as would occur in a perfectly brittle material. This phenomenon is known as tensile strain-softening. In this study, the bilinear curve shown in Fig. 6 was adopted to represent tensile strain-softening in which $\varepsilon_{cr} = f_t'/E_c$, $\varepsilon_{cu} = \alpha_1 \varepsilon_{cr}$ and $\alpha_1 = 10$–25 (Huang et al. 2003).
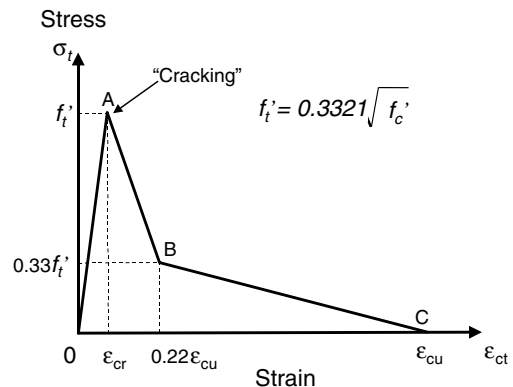

Fig. 6. Concrete tension curve used in the model

Concrete experiences load-induced thermal strain (LITS) under fire conditions. The LITS is the strain that cannot otherwise be accounted for because of the decomposition of the cement paste. It occurs under compressive stress as temperature increases, is essentially permanent, unrecoverable, and only occurs under initial heating. The LITS is temperature-dependent and independent of time. Previous research (Huang et al. 2009) indicated that the LITS has significant impact on the structural behavior of reinforced concrete column in fire. However, the effect of the LITS on the behavior of reinforced concrete beam is considerably less compared to columns. This is because, for the bending member, the LITS exists only in the region subjected to compressive stresses (top part of the cross section). Another issue is that at present a reliable model for calculating the LITS is lacking. Therefore, for reinforced concrete slabs, the LITS has not taken into account in the current model.

Working Procedure of the Current Model

In this study, for modeling of crack evolution at the earlier stage of the analysis, the smeared crack model was used. At the later stage of the analysis, the delayed XFEM (D-XFEM) was used to calculate the individual through-the-thickness cracks' opening within the largely deformed slab elements. Therefore, in order to combine the
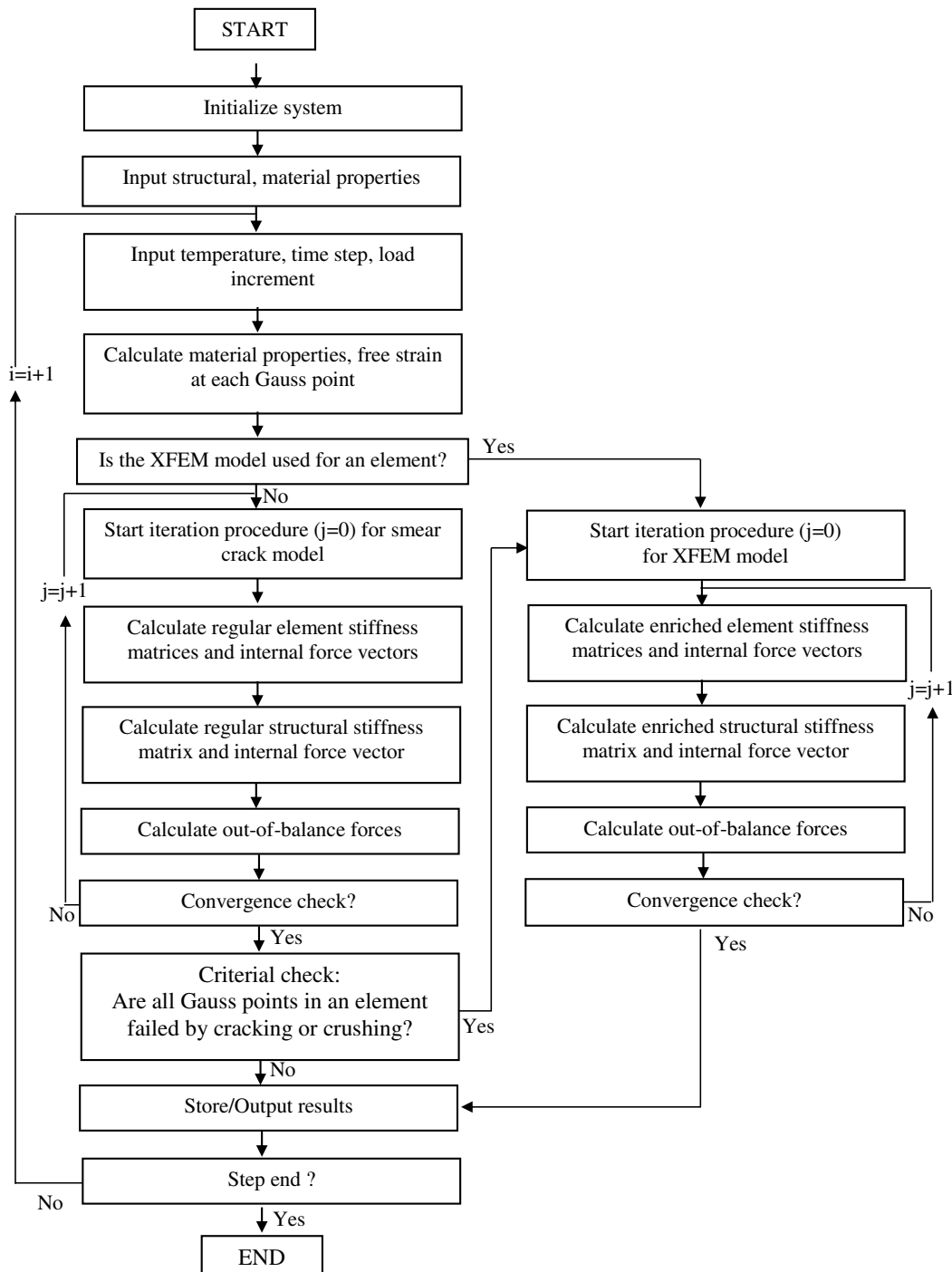
Fig. 7. Flowchart of the current model

smeared crack model with the D-XFEM model into a hybrid FE procedure, a criterion was developed here to determine the shift from the smeared crack model to the XFEM model. That is, when all integration points within a slab element fail because of cracking or crushing assessed by the smeared crack model, that element will be enriched, and the extended strong discontinuity will be introduced into that element. The reason for the proposed criterion is that once all integration points have failed by cracking or crushing, the slab concrete almost entirely loses its stiffness, and thus large deformation will appear in the slab, so it is reasonable to assume the through-the-thickness cracks have been formed in that slab element. For the element enriched, the XFEM formulations were used to calculate the element stiffness matrix and internal force vector. The working procedure of the current model is as the following:

Fig. 7 shows the flowchart of the current model. At the beginning of the analysis, all plain concrete slab elements were modeled regularly by using the smeared crack model. Each node was assumed to have 12 DOFs including 6 regular DOFs and 6 additional DOFs. For the smeared crack element, only regular DOFs were activated, and all parameters related to additional DOFs were set to zero. Over each incremental loading step, the regular slab elements (using the smeared crack model) were examined one by one, and when all integration points within a certain regular slab element failed by cracking based on the smeared crack model, then that element was enriched by introducing an extended strong discontinuity. All parameters of that element were replaced by the parameters of an XFEM element and two additional membrane's DOFs (u_i^a, v_i^a) per node were activated. The element stiffness matrix $\mathbf{K}$ and internal force vector $\mathbf{Q}^e$ of the enriched element were calculated using the model presented in previous sections.

In this study, for defining the orientation of an individual through-the-thickness crack within an enriched element, it is reasonable to assume that the crack orientations of each layer were generally unchanged along the thickness of the slab and were consistent with the initial crack orientation of the bottom layer. Hence, the cracking orientation of an enriched element was defined as the cracking orientation at the central fifth integration point of the bottom layer of the element, predicted by the smeared crack model.

As mentioned before, in this research the shifted enrichment function was used, the field of discontinuous displacement vanished outside the element that enclosed the crack. Hence, only the elements cutting by the crack were enriched. Fig. 8 illustrates the enriched elements and enriched nodes, in which the regular elements using the smeared crack model are hollow, the enriched elements are filled with grey color, the solid circles represent the enriched nodes, and the hollow circles indicate regular nodes. In the current model, only one crack was allowed in an element. Fig. 9 illustrates the mechanism of a crack initiating and propagating. As shown in the figure, there are two ways that an initial crack cut a quadrilateral element, Initial Crack 1 in Fig. 9(a) and Initial Crack 2 in Fig. 9(b), each of which has possibly three crack propagation paths within the next element when the initial crack extends from the existing crack tip at Element 1 into Element 2.

For calculating the stiffness matrix of the regular slab element using the smeared crack model, 9 Gauss integration points were adopted. However, for the enriched slab element with the extended strong discontinuity, conventional 9 Gauss integration points were not sufficient to identify the enrichment function from a constant function over different sides (Ω^+ and Ω^-) of a discontinuity (Wells and Sluys 2001). Hence, the enriched elements were integrated separately on each side of the discontinuity. In this study, the element was partitioned into subtriangles. As shown in Fig. 10, 7 Gauss points were used for each subtriangle. And for an enriched element, a total of 56 Gauss points were used. As shown in Fig. 10(a), a
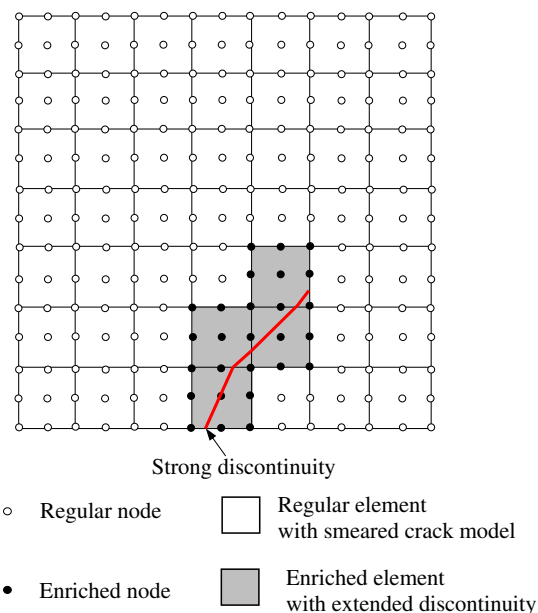

Fig. 8. Regular elements and enriched elements in the slab model
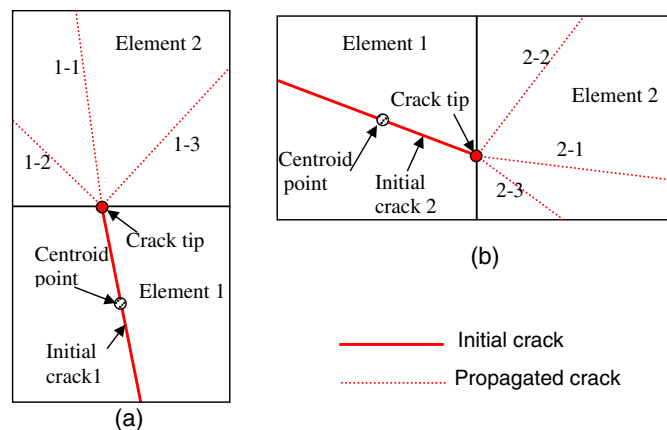

Fig. 9. Crack initiation and propagation

quadrilateral element was cut by a crack into two subquadrilaterals, and four subtriangles with 28 Gauss points were applied within each subquadrilateral. Fig. 10(b) shows a quadrilateral element cut by a crack into a pentagon and a triangle. In this case, 35 Gauss points distributed over 5 subtriangles were applied within the pentagon, and 21 Gauss points distributed over 3 subtriangles were applied within the triangle.

Bond-Link and Reinforcing Steel Bar Elements

Fig. 1 shows a RC slab modeled as an assembly of three different elements (plain concrete, reinforcing steel bar, and bond-link elements). A three-dimensional three-node beam element (Huang et al. 2009) was adopted here to represent the reinforcing steel bar, in which both material and geometric nonlinearities are considered. Normally, in the numerical modeling of reinforced concrete members, a two-node truss element can be used to represent the reinforcing steel bar. However, because the truss element ignores the bending degrees of freedom, the steel bars are only approximately modeled using this kind of element. Hence, the beam
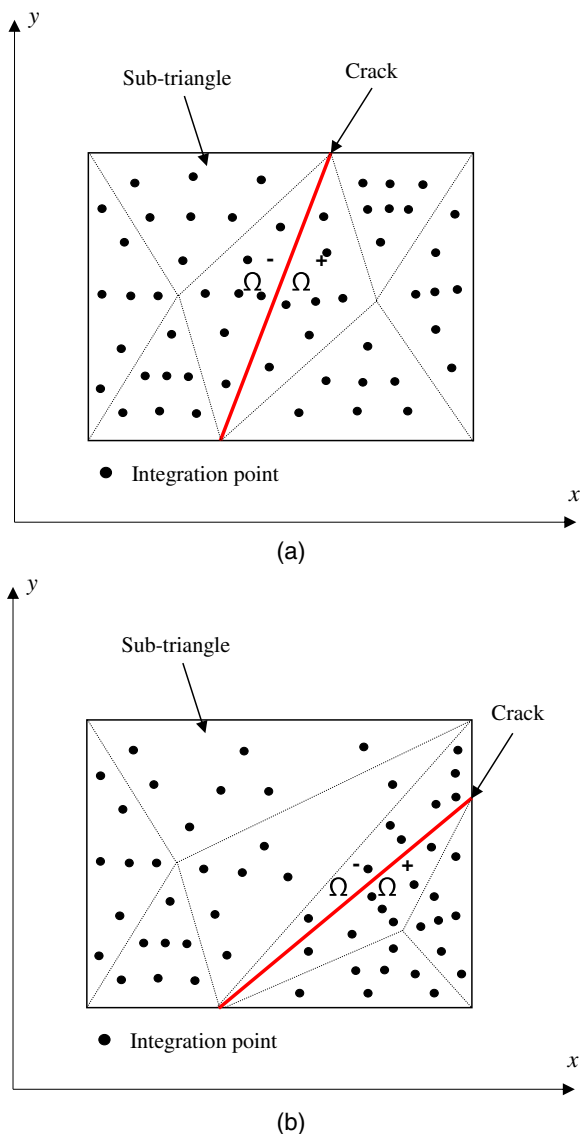
(a)

(b)

Fig. 10. Integration scheme for an enriched element: (a) crack cutting a concrete element into two quadrilaterals; (b) crack cutting a concrete element into a pentagon and a triangle

Fig. 11. High temperature stress–strain relationships of reinforcing steel

Fig. 12. Bond-link element

element can more accurately model reinforcing steel bars compared to the truss element. The cross section of the beam element was divided into a matrix of segments, and each segment might have different material, temperature, and mechanical properties. The models defined in EN1992-1-2 (Commission of the European Communities 2004) were used to calculate the steel mechanical properties and thermal elongation. Fig. 11 shows the stress-strain curve of reinforcing steel at elevated temperatures suggested by EN1992-1-2 (Commission of the European Communities 2004), in which the effect of creep of steel bar has been considered implicitly.

For modeling the interaction between the reinforcing steel and the concrete within the RC slabs, a bond-link element developed by the second author (Huang 2010a) was used. As shown in Fig. 12, the bond-link element links the nodes between a plain concrete slab element and steel bar element. The bond element is a specialized two-node element of zero length, which has three translational degrees of freedom u, v, w and three rotational degrees of freedom θ_x, θ_y, θ_z at each node, where x, y, z are local coordinates of a
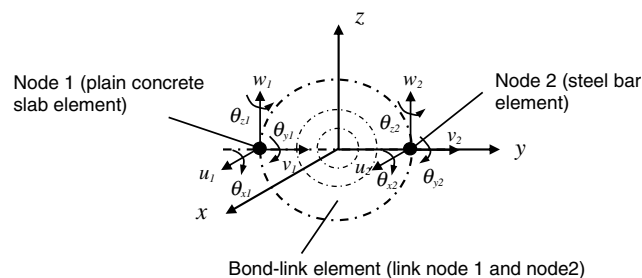
reinforcing steel element in which x is the direction of the longitudinal axis of the reinforcing steel element. It was assumed that the slip between reinforcing steel and concrete was related only to the longitudinal axis direction (x-direction). The effects of various influencing factors such as the type of steel bar (ribbed or smooth) and the concrete strength were considered in the model. Also the bond strength was degraded at elevated temperatures. The detailed formulations can be found in Huang (2010a).

In the current model a reinforced concrete slab was modeled as an assembly of finite plain concrete slab, reinforcing steel bar, and bond-link elements (Fig. 1). For the plain concrete slab elements, after multiple cracks formed within the elements the forces originally resisted by the plain concrete slab elements could be transferred into the reinforcing steel bar element through bond-link elements. Hence, the modeling behavior of a reinforced concrete slab was much smoother compared to modeling of plain concrete slab only. A load control with the full Newton-Raphon solution procedure used in the current model is robust enough to deal with these convergence problems. The numerical stability of the current model is very good, and the analysis can be performed until the fracture of reinforcing steel bars or the failure of bond-link elements.

Thermal Analysis of Reinforced Concrete Slabs in Fire

A computer program *FPRCBC-T* was developed by the second author (Huang et al. 1996; Huang 2010b) for predicting the temperature history across the cross sections of reinforced concrete

members under fire conditions. This thermal model was based on a two-dimensional nonlinear finite-element procedure. In this model, the thermal properties of concrete were considered as temperature and moisture dependent, and the thermal properties of steel were temperature dependent. The effect of water evaporation in concrete was considered in the model. In the thermal analysis, performed using *FPRCBC-T*, the fire conditions were described by time-temperature curves of the fire at some distance away from the member. For this purpose, convection and radiation boundary conditions were used to simulate the heat transfer between the fire and the surfaces of the members that were exposed to the fires. For the thermal analysis of the reinforced concrete slab, the slab could be divided into layers along the thickness of the slab for predicting the temperature distribution within the cross section of the slab. The detailed formulations of the model can be found in Huang et al. (1996).

Validations

Mesh Sensitivity Test

For investigating the influence of mesh size, a square reinforced concrete slab with simply supported condition at room temperature was analyzed using different sizes of mesh, i.e. coarser mesh (36 plate elements of plain concrete, 72 elements of steel bar and 156 bond-link elements) and finer mesh (144 plate elements of plain concrete, 288 elements of steel bar and 600 bond-link element), respectively. The slab with the dimension of $1,100 \times 1,100 \times 19.1$ mm was reinforced by single layer steel bars with diameter of 2.42 mm at space of 50 mm. The yield strength of steel bar was 732 MPa, and the concrete compressive strength at ambient temperature used in the modeling was 38 MPa. The comparisons of predicted loads versus deflection curve and cracking patterns by using different meshes are given in Figs. 13 and 14, respectively. It is evident that the current model is not very sensitive to the mesh sizes in terms of both deflection and cracking pattern.

Modeling Reinforced Concrete Slabs in Fire

For validating the current model, four fire tests of RC slabs were modeled. These fire tests on RC slabs conducted by Bailey and Toh (2007) were carried out under a transient heating state with a
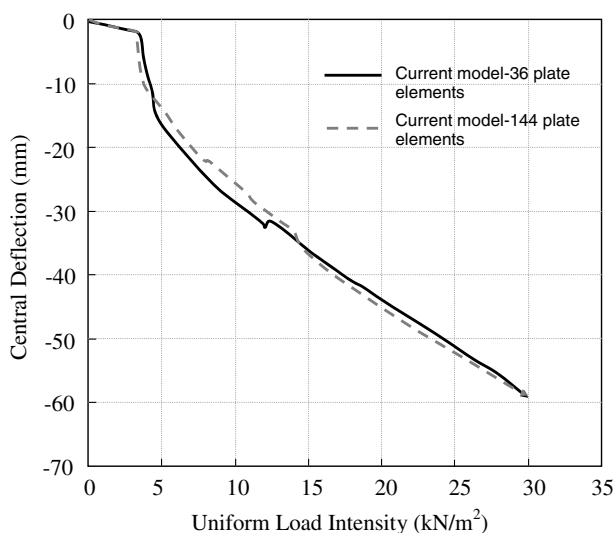
uniform working load (*P*) applied on the top surface of the slab. The applied load remained constant during the heating process. Here the four slabs, designated as MF1, MF2, MF3, and MF4, were modeled. As shown in Fig. 15, all slabs were reinforced by a single layer reinforcement in each direction and have 5 mm cover to steel bars in long span. The measured concrete's compressive strengths at room temperature were $f'_c(20°C) = 43.2$ MPa (MF1), $f'_c(20°C) = 43.3$ MPa (MF2), $f'_c(20°C) = 39.1$ MPa (MF3), and $f'_c(20°C) = 39.0$ MPa (MF4). In the validations, the tested material properties were used. All cases were modeled using both the smeared crack model and the current model for comparison purpose.

Both Slabs MF1 and MF3 were rectangular slabs and had dimensions of $1,700 \times 1,100$ mm with thicknesses of 19.7 mm and 19.0 mm, respectively. Slab MF1 was reinforced by steel bars with diameter of 2.43 mm and yield strength of 695 MPa in the long span, and with diameter of 2.41 mm and yield strength of 722 MPa in the short span, respectively. The spacing of reinforcing bars was 50.8 mm in both sp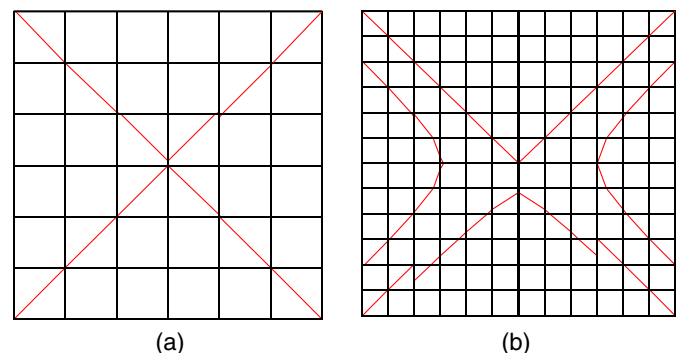ans. Slab MF3 was reinforced by steel bars with diameter of 1.54 mm and spacing of 25.4 mm in both spans. The yield strength of reinforcing bars for MF3 was 695 MPa in the long span and 722 MPa in the short span. The applied load *P* for MF1 and MF3 was 5.28 and 3.66 kN/m², respectively.

The dimensions of square slabs MF2 and MF4 were $1,100 \times 1,100$ mm, and the thicknesses were 23.1 mm and 19.8 mm, respectively. Slab MF2 was reinforced by steel bars with diameter of 2.41 mm and yield strength of 684 MPa in the long span, and with diameter of 2.43 mm and yield strength of 780 MPa in the short span, respectively. The spacing of reinforcing bars was 50.8 mm in both spans. Slab MF4 was reinforced by steel bars

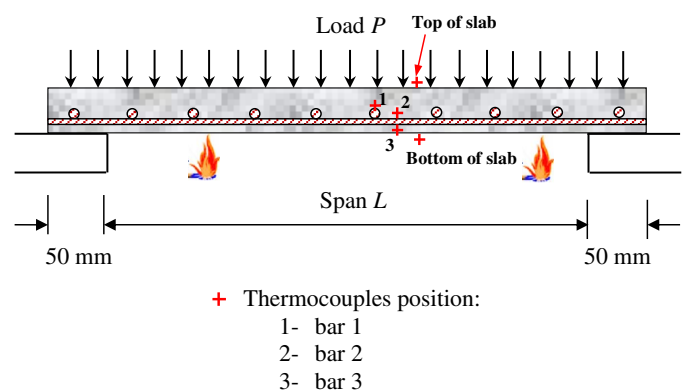**Fig. 14.** Predicted cracking patterns using different size of mesh: (a) 36 plate elements; (b) 144 plate elements

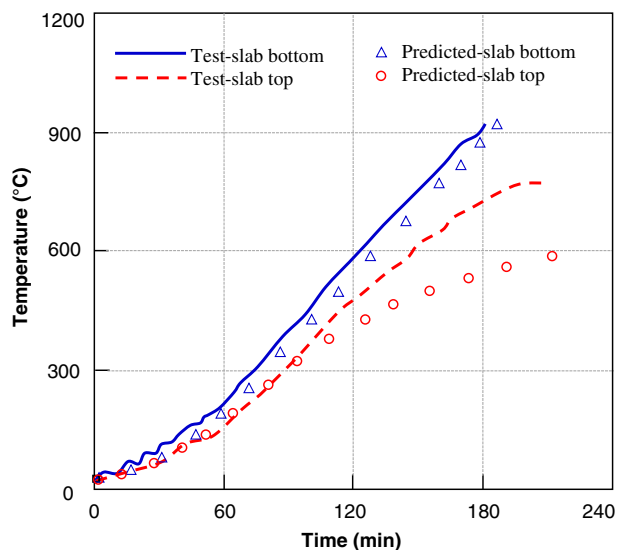**Fig. 15.** Details of tested reinforced concrete slabs under fire conditions (adapted from Bailey and Toh 2007)
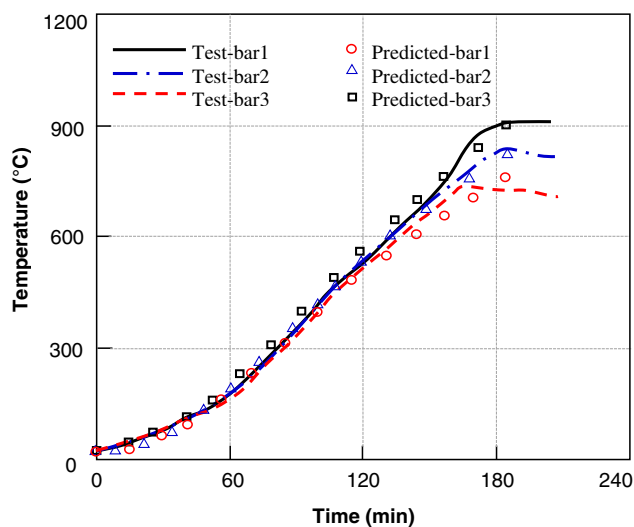

Fig. 13. Predicted deflections using different sizes of mesh

Fig. 16. Predicted and measured temperatures of Slab MF1

Fig. 17. Predicted and measured temperatures of reinforcing bars (MF1)

Fig. 18. Predicted and measured maximum deflections of Slab MF1
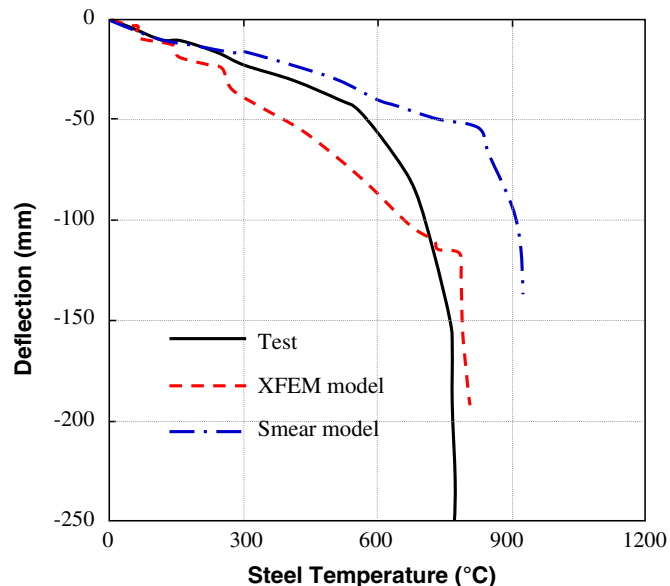
Fig. 19. Predicted and measured maximum deflections of Slab MF2

with diameter of 1.54 mm and space of 25.4 mm in both spans. The yield strength of reinforcing bars for MF4 was 336 MPa in the long span, and 349 MPa in the short span. The applied load P for MF2 and MF4 was 5.52 and 5.43 kN/m^2, respectively.

For modeling a RC slab in fire, the thermal analyses of the slab need to be done first. The results of the thermal analysis were then used as the temperature inputs to conduct structural analysis. The sizes of layers along the thickness of the slabs used for the thermal analysis were also used for the structural analysis, and all modeled slabs were subdivided into ten layers along the thickness of plain concrete slabs for both thermal and structural analyses.

Fig. 16 illustrates the predicted temperatures against tested results for bottom surface and top surface of Slab MF1. Fig. 17 compares the predicted and tested temperatures for reinforcing steel bar layers, where Bar 1, Bar 2, and Bar 3 represent the temperatures of the top surface, midsurface, and bottom surface of steel bar layers, respectively (Fig. 15). Good agreements have been achieved between the tests and predictions for the temperatures of the bottom
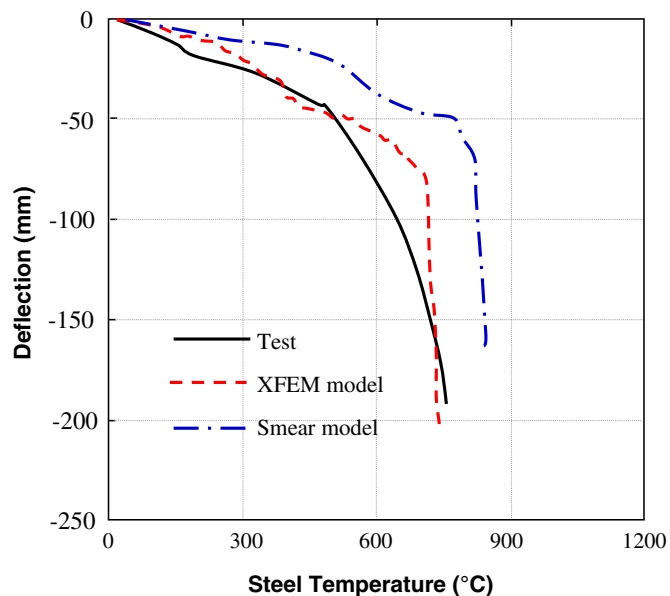
surface of concrete and the reinforcing steel bars. The predicted temperatures of the top surface of concrete are lower than the measured results after heating for about 120 min. This is probably because the effect of big individual cracks on heat transfer over the thickness of the slab tended to cause the increase of temperature on the top surface of concrete, and this phenomenon was not considered in the thermal analysis. However, because the structural response of reinforced concrete slabs mainly relies on the capacity of reinforcement at elevated temperatures, it is acceptable to use the predicted temperature histories given in Figs. 16 and 17 for the structural analysis of the slabs.

Figs. 18–21 show the comparisons of predicted and tested load-central deflection curves for Slabs MF1, MF2, MF3, and MF4. The deflections predicted by the current model are in good agreement with the test data. The predictions of the current model are better
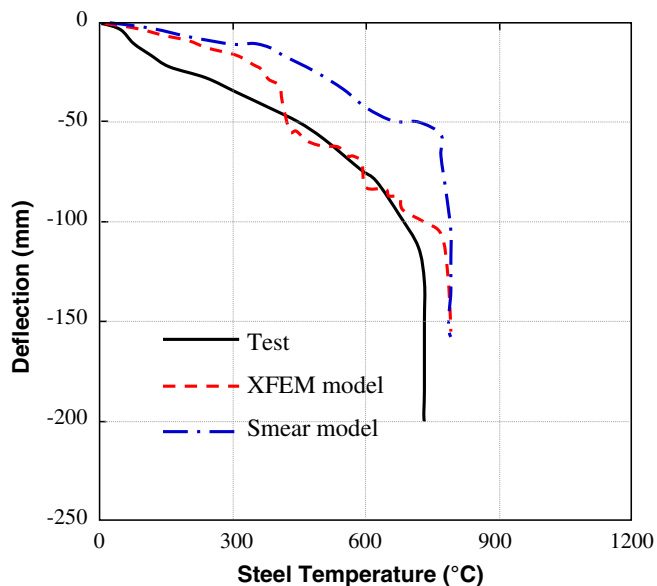
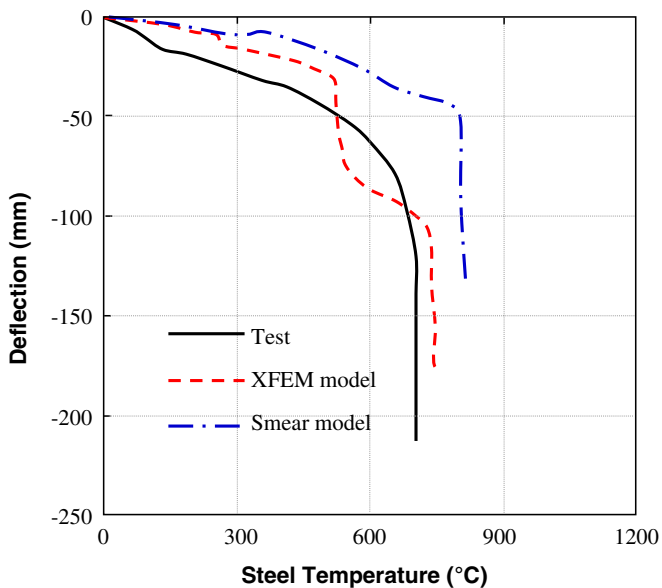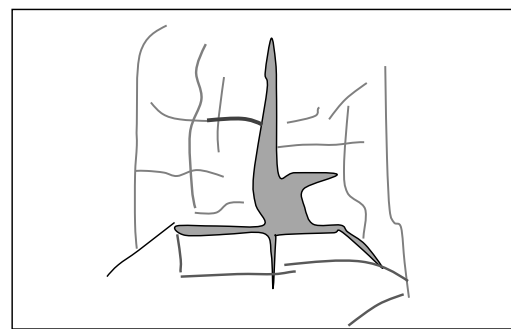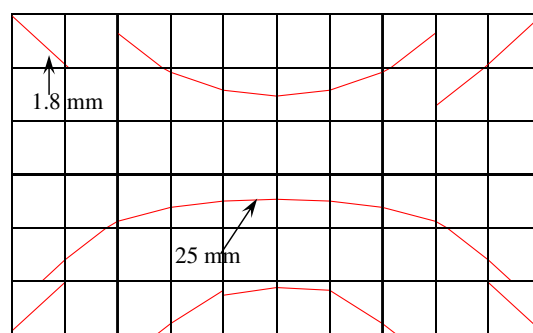**Fig. 20.** Predicted and measured maximum deflections of Slab MF3

Fig. 21. Predicted and measured maximum deflections of Slab MF4

Fig. 22. Predicted and measured cracking patterns of MF1 (unit: millimeters): (a) tested; (b) predicted

Fig. 23. Predicted and measured cracking patterns of MF2 (unit: millimeters): (a) tested; (b) predicted

than the predictions of the smeared crack model. Therefore, the model presented in this paper is capable of predicting the global response of reinforced concrete slabs in fire.

Figs. 22 and 23 present the predicted cracking patterns of Slabs MF1 and MF2, respectively. The predicted cracking patterns are similar to the tested results. The predicted cracking patterns are reasonable as they basically agree with the yield-line pattern of the slab. For Slab MF1, the predicted cracks near corners evolved diagonally, and those near central area tended to propagate horizontally, where the biggest crack (with an opening of 25 mm) occurred near the central part of the slab, and the smallest crack (with an opening of 1.8 mm) appeared near the corner. For Slab MF2, the predicted cracks propagated diagonally and crossed through the whole slab. The crack opening at the central part of the slab reached around 41 mm although there were also some minor cracks in the slab—for instance, a crack with a small opening of 3.4 mm
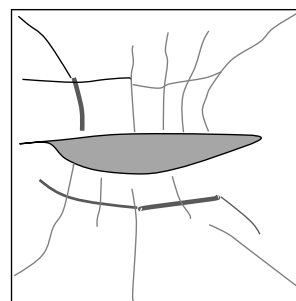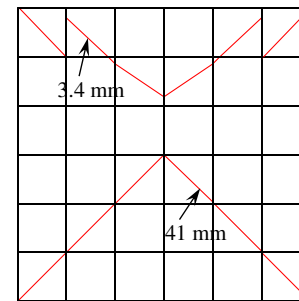
appeared near the corner of the slab. This shows that the opening of localized cracks within a RC slab can be reasonably predicted by the current model. Some predicted crack patterns show crack discontinuity over small offsets (Fig. 22, the upper side of left bottom corner element). This is because, when two cracks originated from different regions propagate toward each other and then intersect at the common side of two neighboring elements, the predicted crack orientations make the two crack tips slightly offset from each other instead of intersecting at the same point.

Note that in the case of Slab MF1, the current model didn't successfully model the observed big crack crossing throughout the short span of the slab. This is because the current model only allows one strong discontinuity in each element; the elements that had been enriched once to hold the horizontal strong discontinuity couldn't be enriched again to accommodate the second strong discontinuity (vertical crack). Previous research has been carried out to

model intersecting cracks by XFEM (Daux et al. 2000). However, because there are often many cracks existing in a reinforced concrete slab, tracing the propagations of all intersecting cracks can be very complex. This will be a subject of further research.

The validations show that the computational time of the current model is efficient and has the same order compared to the original slab model, which is based on the smeared crack approach. Therefore it is feasible to use the current model for modeling full-scale slab fire tests. The original slab model has been adopted by the commercial fire engineering design software *VULCAN* for structural fire engineering design of steel-framed composite buildings. Hence, for larger composite buildings in fires, both structural stability and integrity of RC floor slabs can be assessed by the current model.

Conclusions

This paper presents a hybrid layered FE model for predicting the initiation and propagation of individual large through-the-thickness cracks within RC floor slabs at elevated temperatures. In this model the reinforced concrete slabs were modeled as an assembly of three different elements (plain concrete, reinforcing steel bar, and bond-link elements). A hybrid FE procedure that combines the smeared crack model with XFEM was developed. The early stages of crack evolution were modeled by the smeared crack model. In the later stages of the analysis, the individual big cracks within the largely deformed RC floor slabs were captured using D-XFEM. For determining the shift from smeared crack model to XFEM formulations, a robust criterion has been proposed.

The proposed hybrid nonlinear FE procedure has been validated successfully against fire tests of RC slabs. It is reasonable to conclude that the current model provides for the first time a robust model to assess both structural stability and integrity of RC slabs in fire.

Acknowledgments

Notation

The following symbols are used in this paper:

$\mathbf{B}^a$ = enriched strain-displacement transformation matrix;
$\mathbf{B}^u$ = regular strain-displacement transformation matrix;
$\mathbf{D}$ = plain concrete constitutive matrix;
$\mathbf{f}^{\text{ext}}$ = external force vector of an element;
$\mathbf{Q}^a$ = enriched internal force vector of an element;
$\mathbf{Q}^u$ = regular internal force vector of an element;
$\mathbf{K}^{aa}$ = enriched stiffness matrix of an element;
$\mathbf{K}^{uu}$ = regular stiffness matrix of an element;
$sign(x)$ = sign function;
$\mathbf{u}_{\text{cont}}$ = vector of continuous displacement field;
$\mathbf{u}_{\text{dis}}$ = vector of discontinuous displacement field; and
$\Psi_i(\mathbf{x})$ = enrichment function.

References

Areias, P. M. A., and Belytschko, T. (2005). "Non-linear analysis of shells with arbitrary evolving cracks using XFEM." *Int. J. Numer. Methods Eng.*, 62(3), 384–415.

Bailey, C. G., and Toh, W. S. (2007). "Small-scale concrete slab tests at ambient and elevated temperatures." *Eng. Struct.*, 29(10), 2775–2791.

Belytschko, T., and Black, T. (1999). "Elastic crack growth in finite elements with minimal remeshing." *Int. J. Numer. Methods Eng.*, 45(5), 601–620.

Bentley, P. K., Shaw, D., and Tomlinson, L. (1996). "ECSC project: Behavior of a multistory steel framed building subjected to natural fires. Test 3: Corner compartment. Data files: Deflection/displacement measurements." *Rep. No. S423/3/Part D1*, Swinden Technology Centre, Rotherham, U.K.

Bordas, S., Nguyen, P. V., Dunant, C., Guidoum, A., and Nguyen-Dang, H. (2007). "An extended finite element library." *Int. J. Numer. Methods Eng.*, 71(6), 703–732.

Budyn, É., Zi, G., Moës, N., and Belytschko, T. (2004). "A method for multiple crack growth in brittle materials without remeshing." *Int. J. Numer. Methods Eng.*, 61(10), 1741–1770.

Commission of the European Communities. (2004). "Eurocode 2, design of concrete structures. 1.2: General rules—Structural fire design." *EN 1992-1-2*, Brussels, Belgium.

Daux, C., Moës, N., Dolbow, J., Sukumar, N., and Belytschko, T. (2000). "Arbitrary branched and intersecting cracks with the extended finite element method." *Int. J. Numer. Methods Eng.*, 48(12), 1741–1760.

Dolbow, J., Moës, N., and Belytschko, T. (2000). "Modeling fracture in Mindlin-Reissner plates with the extended finite element method." *Int. J. Solids Struct.*, 37(48–50), 7161–7183.

Foster, S. J. (2006). "Tensile membrane action of reinforced concrete slabs at ambient and elevated temperatures." Ph.D. thesis, Univ. of Sheffield, Sheffield, U.K.

Huang, Z. (2010a). "Modelling the bond between concrete and reinforcing steel in a fire." *Eng. Struct.*, 32(11), 3660–3669.

Huang, Z. (2010b). "The behaviour of reinforced concrete slabs in fire." *Fire Saf. J.*, 45(5), 271–282.

Huang, Z., Burgess, I. W., and Plank, R. J. (2003). "Modelling membrane action of concrete slabs in composite buildings in fire. I: Theoretical development." *J. Struct. Eng.*, 10.1061/(ASCE)0733-9445(2003) 129:8(1093), 1093–1102.

Huang, Z., Burgess, I. W., and Plank, R. J. (2009). "Three-dimensional analysis of reinforced concrete beam-column structures in fire." *J. Struct. Eng.*, 10.1061/(ASCE)0733-9445(2009)135:10(1201), 1201–1212.

Huang, Z., Platten, A., and Roberts, J. (1996). "Non-linear finite element model to predict temperature histories within reinforced concrete in fires." *Build. Environ.*, 31(2), 109–118.

Izzuddin, B. A., and Elghazouli, A. Y. (2004). "Failure of lightly reinforced concrete members under fire I: Analytical modelling." *J. Struct. Eng*, 10.1061/(ASCE)0733-9445(2004)130:1(3), 3–17.

Kodur, V. K. R., and Bisby, L. A. (2005). "Evaluation of fire endurance of concrete slabs reinforced with fiber-reinforced polymer bars." *J. Struct. Eng.*, 10.1061/(ASCE)0733-9445(2005)131:1(34), 34–43.

Kodur, V. K. R., and Shakya, A. M. (2017). "Factors governing the shear response of prestressed concrete hollowcore slabs under fire conditions." *Fire Saf. J.*, 88, 67–88.

Kupfer, H. B., and Gerstle, K. H. (1973). "Behavior of concrete under biaxial stresses." *J. Eng. Mech. Div.*, 66(8), 853–866.

Lasry, J., Pommier, J., Renard, Y., and Salaün, M. (2010). "eXtended finite element methods for thin cracked plates with Kirchhoff-Love theory." *Int. J. Numer. Methods Eng.*, 84(9), 1115–1138.

Liao, F., and Huang, Z. (2015). "An extended finite element model for modelling localized fracture of reinforced concrete beams in fire." *Comput. Struct.*, 152(5), 11–26.

Lim, L., Buchanan, A., Moss, P., and Franssen, J. M. (2004). "Numerical modelling of two-way reinforced concrete slabs in fire." *Eng. Struct.*, 26(8), 1081–1091.

Melenk, J. M., and Babuŝka, I. (1996). "The partition of unity finite element method: Basic theory and application." *Comput. Methods Appl. Mech. Eng.*, 139(1–4), 289–314.

Moës, N., Dolbow, J., and Belytschko, T. (1999). "A finite element method for crack growth without remeshing." *Int. J. Numer. Methods Eng.*, 46(1), 131–150.

Shakya, A. M., and Kodur, V. K. R. (2015). "Response of precast pre-stressed concrete hollowcore slabs under fire conditions." *Eng. Struct.*, 87(3), 126–138.

Talebi, H., Silani, M., Bordas, S., Kerfriden, P., and Rabczuk, T. (2014). "A computational library for multiscale modeling of material failure." *Comput. Mech.*, 53(5), 1047–1071.

Wells, G. N., and Sluys, L. J. (2001). "A new method for modelling cohesive cracks using finite elements." *Int. J. Numer. Meth. Eng.*, 50(12), 2667–2682.

Wyart, E., Coulon, D., Duflot, M., Pardoen, T., Remacle, J. F., and Lani, F. (2007). "A substructured FE-shell/XFE-3D method for crack analysis in thin-walled structures." *Int. J. Numer. Methods Eng.*, 72(7), 757–779.

Xu, J., Lee, C. K., and Tan, K. H. (2013). "An XFEM plate element for high gradient zones resulted from yield lines." *Int. J. Numer. Methods Eng.*, 93(12), 1314–1344.

Yu, X., and Huang, Z. (2008). "An embedded FE model for modelling reinforced concrete slabs in fire." *Eng. Struct.*, 30(11), 3228–3238.

Zhang, Y. X., and Bradford, M. A. (2007). "Nonlinear analysis of moderately thick reinforced concrete slabs at elevated temperatures using a rectangular layered plate element with Timoshenko beam functions." *Eng. Struct.*, 29(10), 2751–2761.

Zi, G., and Belytschko, T. (2003). "New crack-tip elements for XFEM and applications to cohesive cracks." *Int. J. Numer. Methods Eng.*, 57(15), 2221–2240.